EXPERIMENTAL AND ANALYTICAL INVESTIGATION
OF THE BEHAVIOR OF DIAPHRAGM-THROUGH JOINTS
OF CONCRETE-FILLED TUBULAR COLUMNS

Rong Bin, Chen Zhihua, Zhang Ruoyu, Apostolos Fafitis and Yang Nan

msp

EXPERIMENTAL AND ANALYTICAL INVESTIGATION OF THE BEHAVIOR OF DIAPHRAGM-THROUGH JOINTS OF CONCRETE-FILLED TUBULAR COLUMNS

RONG BIN, CHEN ZHIHUA, ZHANG RUOYU, APOSTOLOS FAFITIS AND YANG NAN

Static tensile loading experiments and nonlinear finite element analysis were carried out to study the mechanical properties and failure modes of diaphragm-through joints of concrete-filled square steel tubular columns. Comparison between experimental data and finite element analysis revealed that the FE predictions of failure modes, load-displacement curves and bearing capacity agree with the test results. It was found that the tensile load from the steel beam flange is mainly shared by the square steel tube and the diaphragm. The plastic zone of the tube appears around the intersections of the tube and the diaphragm whereas the diaphragm plastic zone appears along the cross-section lines enclosed by the steel square tube. Calculation models of yield lines on square steel tube and diaphragm are established based on distribution pattern of plastic zone, and an analytical method for the design of such joints is proposed as well. The experimentally obtained bearing capacities of the tested specimens are in good agreement with the analytically computed capacities.

1. Introduction

Frame structures with concrete-filled square steel tubular columns and H-shaped steel beams have been increasingly used in structural engineering. Inner diaphragm joints and diaphragm-through joints, shown in Figure 1, are two forms of rigid beam-column connections that are used in many applications. In the diaphragm-through method the square tube is disconnected and two diaphragms are placed at the level of the upper and lower flange of the steel beam. The beam is then connected to these diaphragms.

For the inner diaphragm joints, a large number of experimental and theoretical studies [Park et al. 2010; Han et al. 2003; 2008; Fukumoto and Morita 2005; Ricles et al. 2004] have been carried out and calculation methods and formulae [Sasaki et al. 1995; Nie et al. 2005; Zhou et al. 2005] are proposed for the flexural bearing capacity and the shear bearing capacity of inner diaphragm joints. However, for diaphragm-through joints, there is relatively limited research focusing mainly on the seismic performance. Nishiyama et al. [2004] carried low-reversed cyclic loading experiments on 10 specimens of diaphragm-through joints to investigate the failure process. Chen et al. [2006] compared the hysteretic behaviors of inner diaphragm joints and diaphragm-through joints based on low-reversed cyclic loading experimental results and Jiang et al. [2009] studied ductility, energy dissipation and rigidity degradation of diaphragm-through joints by low-reversed cyclic loading experiments.

The flexural bearing capacity is calculated based on the assumption that it depends on the tensile capacity of the panel zone as shown in Figure 2 [Matsui 1985; Morino and Tsuda 2002], and it can be
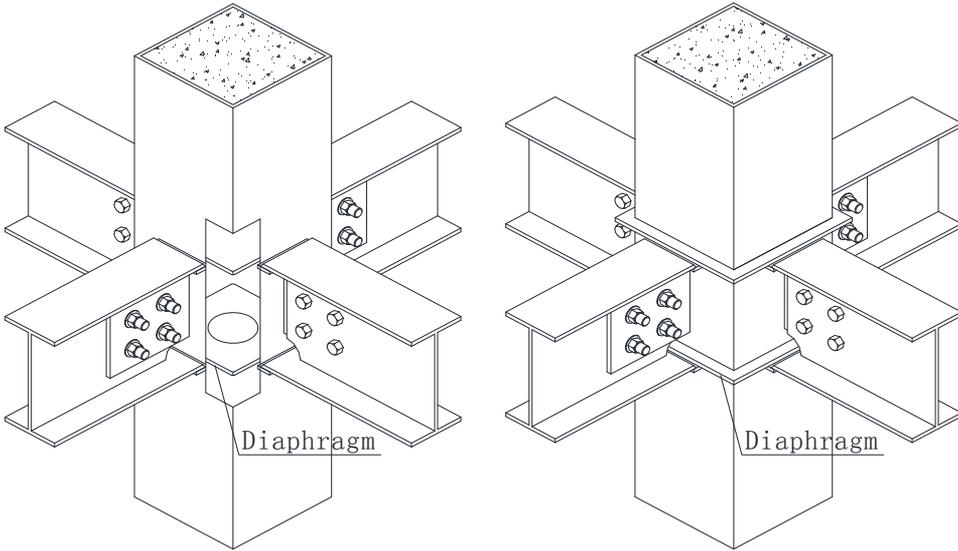
Figure 1. Joint forms: inner diaphragm joint (left) and diaphragm-through joint (right).
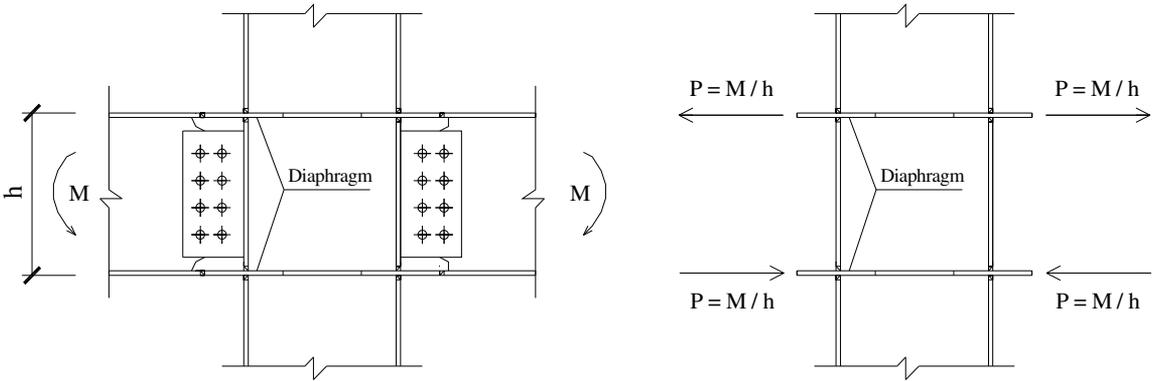
**Figure 2.** Calculation model for flexural bearing capacity of diaphragm-through joints.

expressed as

$$M = P(h - t) \tag{1}$$

where P is the tensile capacity of the panel zone, h is the distance between outer faces of the flanges and t is the thickness of the flange.

In current practice [Fukumoto and Morita 2005] the tensile capacity is evaluated based on two assumed yielding mechanisms of the panel zone. In the first it is assumed that section 1-1, shown in Figure 3, is the yield location and then the yield strength of panel zone is

$$P_{y1}^d = (D + 2h_d - d)t_d f_y^d \tag{2}$$
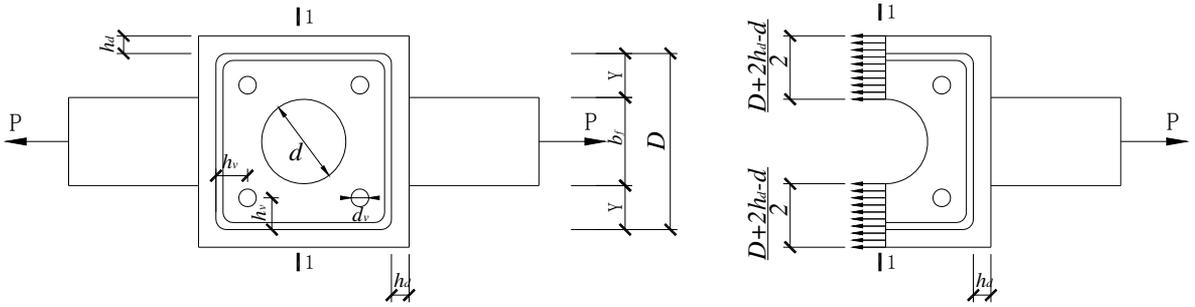
Figure 3. Yield mechanism 1 of diaphragm-through joint.
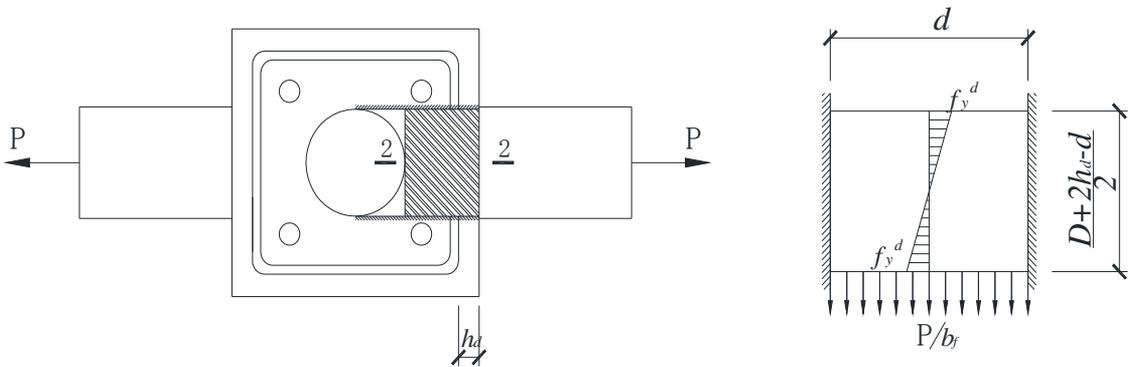
Figure 4. Yield mechanism 2 of diaphragm-through joint.

where D is the width of the square steel tube, h_d is the cantilevered length of the diaphragm, d is the diameter of the central opening for concrete casting, t_d is the thickness of the diaphragm and f_y^d is the yield strength.

In the second mechanism the part of the diaphragm near the central opening is treated as a fixed beam under uniformly distributed load as shown in Figure 4. The width of the beam cross-section equals the thickness of the diaphragm, shown in Figure 4. Assuming that yielding will take place at section 2-2, the yield strength is

$$P_{y2}^d = (D + 2h_d - d)^2 \frac{b_f \cdot t_d}{d^2} f_y^d \tag{3}$$

where b_f is the width of the flange. Note that (3) is a simplifying approximation ignoring the fact that this beam is usually a deep beam.

From (2) and (3), the yield tensile capacity of the panel zone can be expressed as

$$P_y^d = \min(P_{y1}^d, P_{y2}^d). \tag{4a}$$

Substituting the ultimate strength f_u^d of the diaphragm for the yield strength f_y^d of (4a), the ultimate tensile capacity of the panel zone can be expressed as

$$P_u^d = \min(P_{u1}^d, P_{u2}^d). \tag{4b}$$

No experimental data of static tensile loading for diaphragm-through joints were found in the literature. The above mentioned calculation methods for the tensile capacity of diaphragm-through joints ignore the contribution of the tensile capacity of steel tube and the concrete infill. Therefore the yielding mechanism models and the correctness of the results need to be verified by static tensile loading experiments.

The objectives of this investigation are to study the maximum load-bearing capacity and mechanical properties of diaphragm-through joint subjected to static tensile load. The analytical method mentioned above for bearing capacity of diaphragm-through joint under static tensile load is to be examined as well. The main parts of this paper are: firstly to report the experimental results on 8 diaphragm-through joints under static tensile load, secondly to analyze the mechanisms of the diaphragm-through joints subjected to static tensile load by using finite element analysis and thirdly, to establish the yield mechanism model of the joint and to develop an analytical method for the determination of the bearing capacity of diaphragm-through joints under static tensile load.

2. Experimental study

Materials.

(1) Steel tube

Two types of square hollow steel tubes are used to manufacture the specimens. The dimensions of these steel tubes were 250 mm × 250 mm. The thickness was 8 mm and 10 mm respectively. To determine the steel properties of these square tubes, tension coupons are cut and tested in tension. The properties of the tubes are shown in Table 1.

(2) Diaphragm and flange

Two types of steel plates are used to manufacture the diaphragms and the beam flanges with thicknesses 10 mm and 12 mm. The properties of the steel plates are shown in Table 2.

(3) Concrete

Two types of concrete marked by C20 and C40 are used. To determine the concrete material properties, $150 \times 150 \times 150$ mm cubes were cast and cured in conditions similar to that of the experiment and tested in compression. The concrete properties are shown in Table 3.

Dimension (mm)	Thickness (mm)	Yield strength f_y (N/mm^2)	Ultimate strength f_u (N/mm^2)	Modulus of elasticity E (10^5 N/mm^2)	Elongation δ (%)
250 × 250	8	284.7	409.8	2.036	33.6
	10	316.1	463.3	2.180	38.7

Table 1. Material properties of steel tubes.

Thickness (mm)	Yield strength f_y (N/mm^2)	Ultimate strength f_u (N/mm^2)	Modulus of elasticity E (10^5 N/mm^2)	Elongation δ (%)
10	302.8	421.4	1.952	37.4
12	305.2	429.8	2.167	34.6

Table 2. Material properties of steel plates.

| Concrete | Mix proportion (kg/m³) | | | Average crushing | Modulus of |
	Cement	Sand	Coarse aggregate	strength (MPa)	elasticity ($\times 10^4$ MPa)
C20	350	690	1160	25.3	3.46
C40	460	720	1036	47.6	3.73

Table 3. Material properties of concrete.
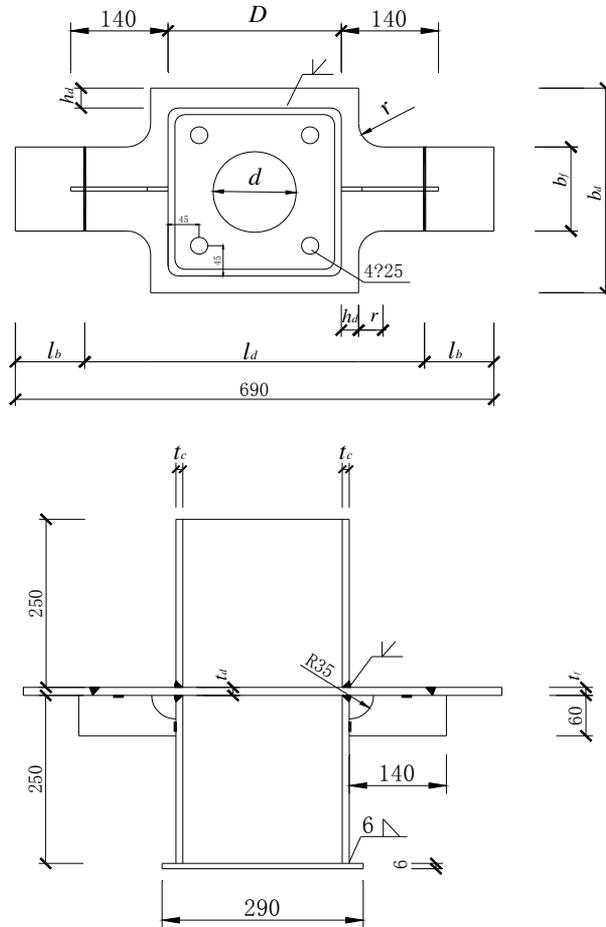
Figure 5. Specimen of tensile loading experiment.

Specimens. Eight diaphragm-through joints of the concrete-filled square steel tubular columns were designed for static tensile loading, as shown in Figure 5. In these specimens, the flange of the steel beam and the diaphragm are connected by butt weld. The stress concentration and the welding stress may have a negative effect on mechanical properties of diaphragm-through joints. Therefore, the arc fillet eliminates the stress concentration effect and sets these butt welds at some distance from the column.

After cutting, the surface is treated by surface grinding machine. The steel tubes, diaphragms and beam flanges are thoroughly wire brushed to remove the rust and loose debris that may be present during

Specimen	Steel tube $D \times t_c$	Flange $l_b \times b_f \times t_b$	Diaphragm $l_d \times b_d \times t_d$	d	r	h_d	Concrete
TR1	250×8	$100 \times 125 \times 10$	$490 \times 300 \times 10$	120	35	25	C40
TR2	250×8	$100 \times 125 \times 10$	$490 \times 300 \times 10$	140	35	25	C40
TR3	250×8	$100 \times 125 \times 10$	$490 \times 300 \times 10$	160	35	25	C40
TR4	250×8	$100 \times 125 \times 12$	$490 \times 300 \times 12$	160	35	25	C40
TR5	250×10	$100 \times 125 \times 12$	$490 \times 300 \times 12$	160	35	25	C40
TR6	250×8	$100 \times 125 \times 10$	$490 \times 300 \times 10$	140	50	25	C40
TR7	250×10	$100 \times 125 \times 12$	$490 \times 320 \times 12$	160	35	45	C40
TR8	250×10	$100 \times 125 \times 12$	$490 \times 300 \times 12$	160	35	25	C20

Table 4. Specimen parameters. All dimensions are in millimeters.

cutting. A steel plate is placed at the bottom of each steel tube prior to filling concrete. The concrete is cured for 28 days. A layer of cement mortar is used to flush the concrete top surface with the steel tube.

The parameters of each specimen are listed in Table 4. The meaning of the symbols D, t_c, l_b, b_f, t_b, l_d, b_d, t_d, d, r and h_d are shown in Figure 5.

Experimental set-up. The specimens of diaphragm-through joints are stretched with clamping conditions at both flange ends using a 1000 kN capacity axial tensile testing machine. A load interval of 50 kN (about one-tenth of the estimated carrying load capacity) is used. Each load interval is maintained for 10 minutes. The response of the specimens is recorded continuously in order to obtain the load-displacement curve. When the load-displacement curve slope changes, it means the specimen enters the yield stage and the loading increment is decreased to 10 kN until failure. The experimental set-up is shown in Figure 6.
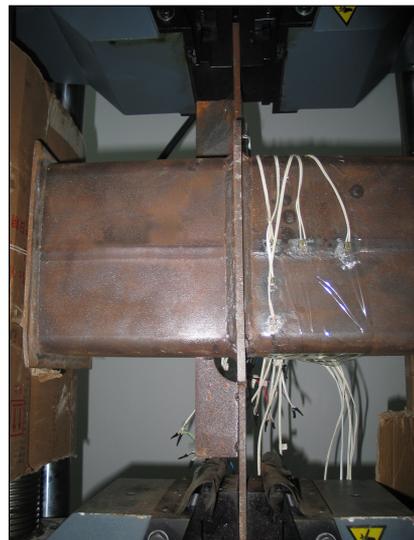
Figure 6. Experimental set-up: axial tensile testing machine (left) and tensile loading (right).

Specimen	Yield load P_y^e (kN)	Failure load P_u^e (kN)	Failure displacement Δ (mm)	Failure mode	Description of failure mode
TR1	361.9	505.8	13.7	flange	Fracture at steel beam flange
TR2	350.7	500.9	14.6	flange	Fracture at steel beam flange
TR3	337.5	462.8	14.7	joint	Local buckling at steel tube Stretching of diaphragm
TR4	396.4	538.9	11.7	joint	Local buckling at steel tube Stretching of diaphragm
TR5	407.8	606.1	17.4	joint	Local buckling at steel tube Stretching of diaphragm
TR6	361.9	504.4	14.1	flange	Fracture at steel beam flange
TR7	416.7	610.0	14.6	joint	Local buckling at steel tube Stretching of diaphragm
TR8	405.7	604.7	18.9	joint	Local buckling at steel tube Stretching of diaphragm

Table 5. Bearing capacity and failure mode.

Results and discussion.

Failure modes. The specimens are loaded up to failure to investigate the mechanical properties and the bearing capacities of the diaphragm-through joints under static tensile loading. A summary of the experimental results such as bearing capacity, displacement and failure modes is given in Table 5. In Table 5, the failure load P_u^e is defined as the maximum strength of specimen. The yield load P_y^e is obtained by a graphical method [Nie et al. 2008]. The failure modes of all specimens can be divided into two types: failure of the flange and failure of the joint (as described Table 5).

In the case of specimen TR6, at the initial stage, there were no obvious deformations in the specimen. When loaded further, plastic necking started to appear at the beam flange. Finally, at failure load, the beam flange was pulled off while there were still no obvious deformations in the diaphragm and the steel tube, as shown in Figure 7, top left. Similar failure was observed in the case of specimens TR1 and TR2.

In the case of specimen TR5, the diaphragm was stretched in the loading direction and the steel tube exhibited signs of local buckling. At the failure point, the deformations of the diaphragm and the steel tube and local buckling were obvious, as shown in Figure 7, top right, and the specimen could not take any more load. After the removal of the concrete from steel tube at the end of the static tensile loading experiment, it could be seen that the circular opening in the center of diaphragm, which is used for concrete casting, is stretch to ellipse, as shown in Figure 7, bottom. Similar failure was observed in the case of specimens TR3, TR4, TR7 and TR8.

Load-displacement curves. All the specimens exhibit the smooth load-displacement curves shown in Figure 8. From these load-displacement curves, it can be seen that specimens have similar behavior. The curves exhibit elastic behavior at the initial stage followed by an inelastic response. All specimens show a clear plastic plateau before the failure point as well as a better ductility.
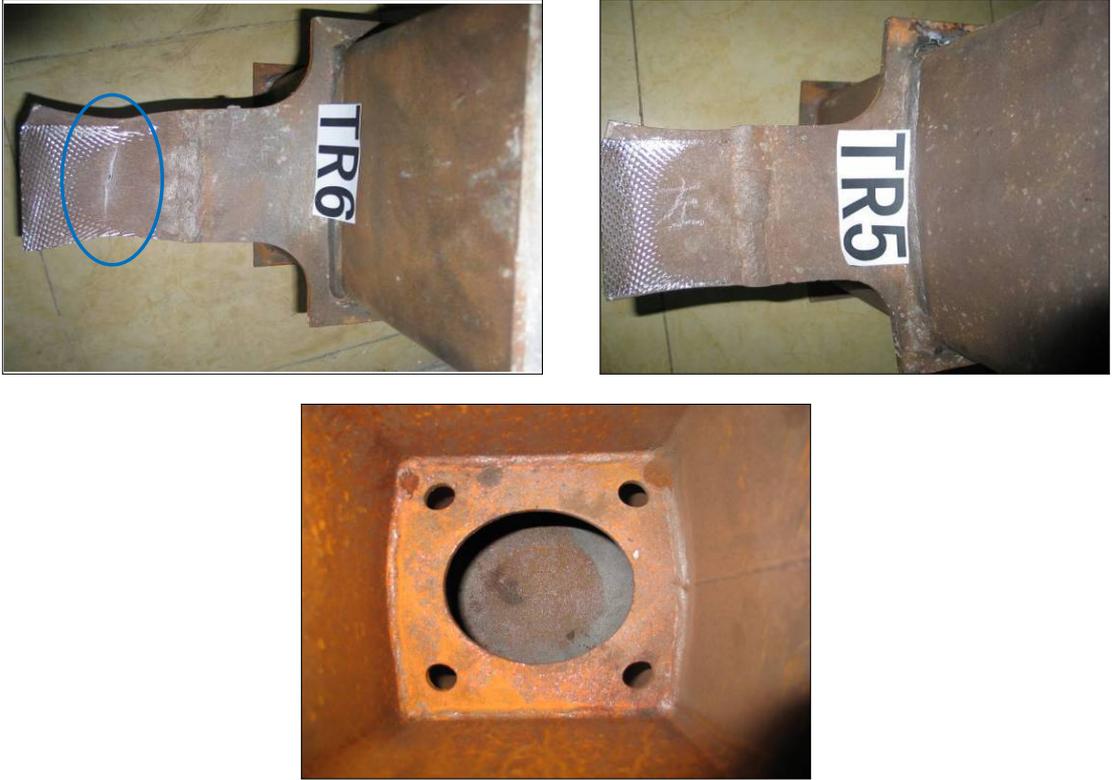
Figure 7. Failure modes. Clockwise from top left: fracture at steel beam flange; local buckling at steel tube; stretching of diaphragm.
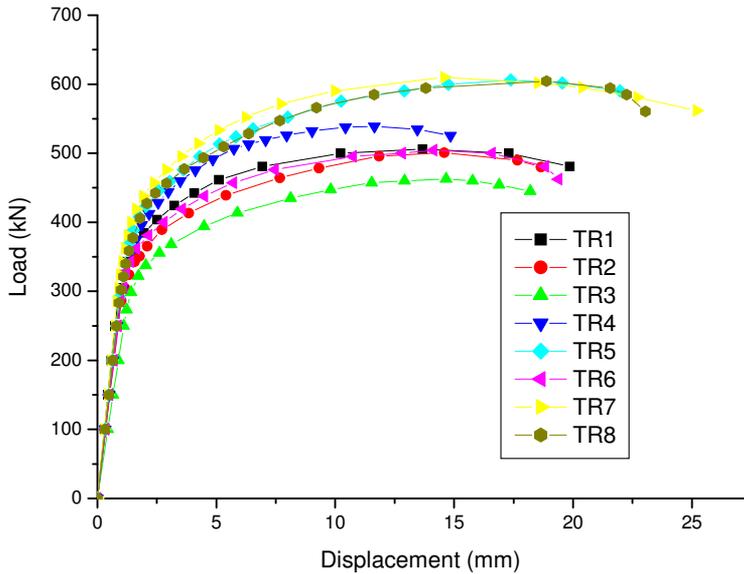

**Figure 8.** Load-displacement curves.
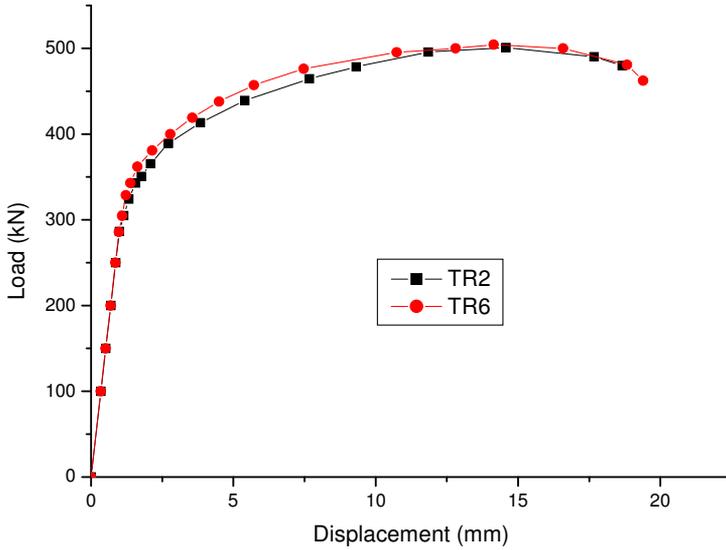
Figure 9. Effect of arc fillet.

The specimens were designed with different parameters such as thickness of steel tube, dimension of diaphragm, radius of arc fillet and concrete and a parametric study was conducted as discussed below.

(1) *Fillet.* In the case of specimens TR2 and TR6, the dimensions and material properties are the same except for the radius r of arc fillet, which is 35 mm for TR2 and 50 mm for TR6. Figure 9 shows the load-displacement comparison between specimens TR2 and TR6. It can be seen that the change of the arc fillet radius from 35 mm to 50 mm does not have an obvious influence in the failure load and the ductility of specimens TR2 and TR6.
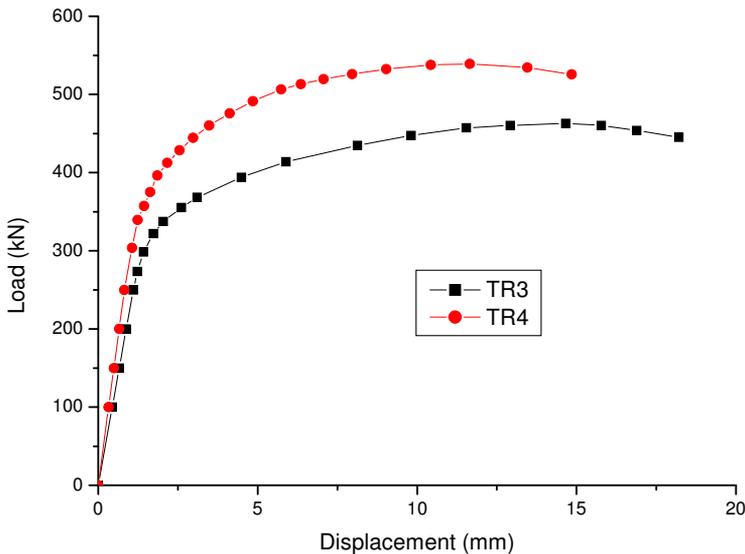
Figure 10. Effect of diaphragm thickness.
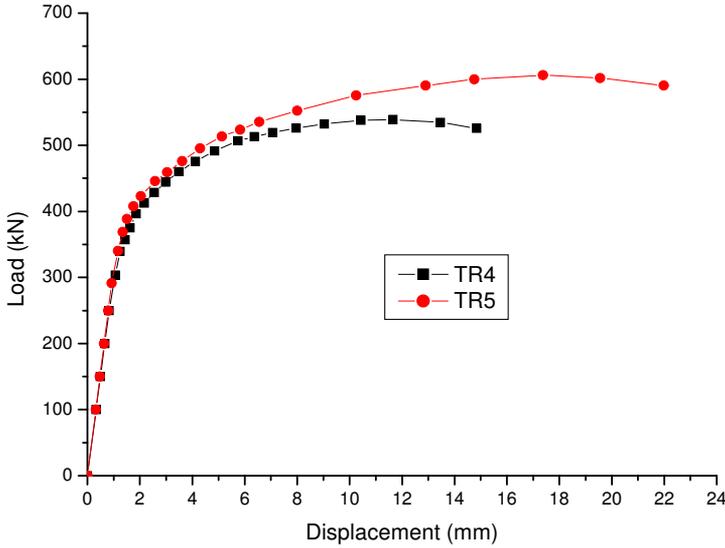
Figure 11. Effect of steel tube thickness.

(2) *Thickness of diaphragm.* In the case of specimens TR3 and TR4, dimensions and material properties are the same except for the thickness t_d of the diaphragm, which is 10 mm for TR3 and 12 mm for TR4. Figure 10 shows the load-displacement comparison between specimens TR3 and TR4. It can bee seen that the larger thickness of the diaphragm lead to a larger failure load.

(3) *Thickness of steel tube.* In the case of specimens TR4 and TR5, dimensions and material properties are the same except for the thickness t_c of steel tube, which is 8 mm for specimen TR4 and 10 mm in TR5. Figure 11 shows the load-displacement comparison between specimens TR4 and TR5. It can be seen that larger thickness of steel tube lead to larger failure load.
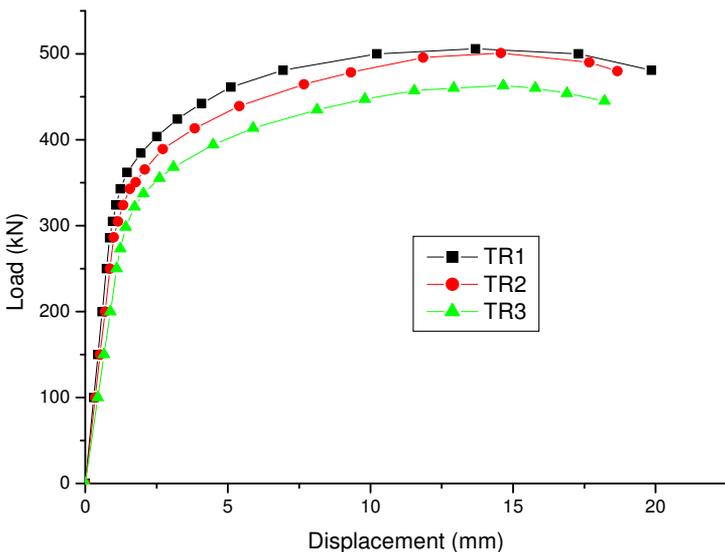
Figure 12. Effect of diameter of central opening in diaphragm.
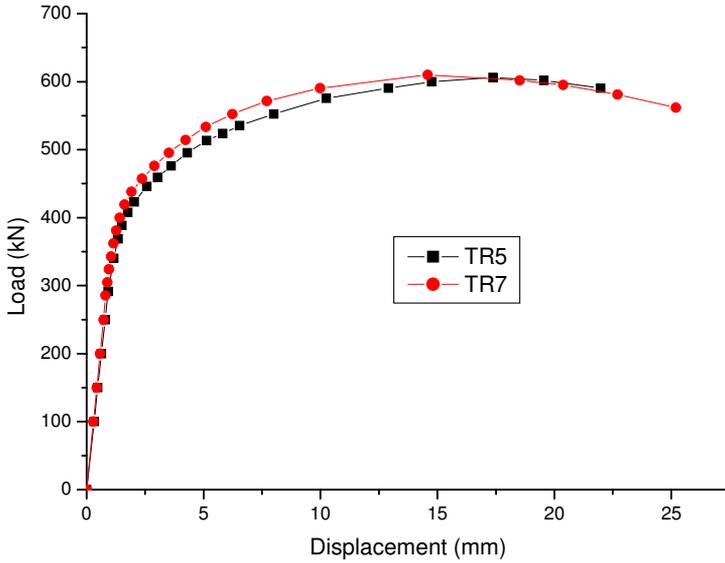
Figure 13. Effect of cantilever length of diaphragm.

(4) *Diameter of central opening in diaphragm.* In the case of specimens TR1, TR2 and TR3, dimensions and material properties are the same except for the diameter *d* of central opening in diaphragm. The diameters *d* of central opening in diaphragms for specimen TR1, TR2 and TR3 are 120 mm, 140 mm and 160 mm, respectively. Figure 12 shows the load-displacement comparison among specimens TR1, TR2 and TR3. It can be seen that larger diameter of central opening in diaphragm lead to smaller failure load.
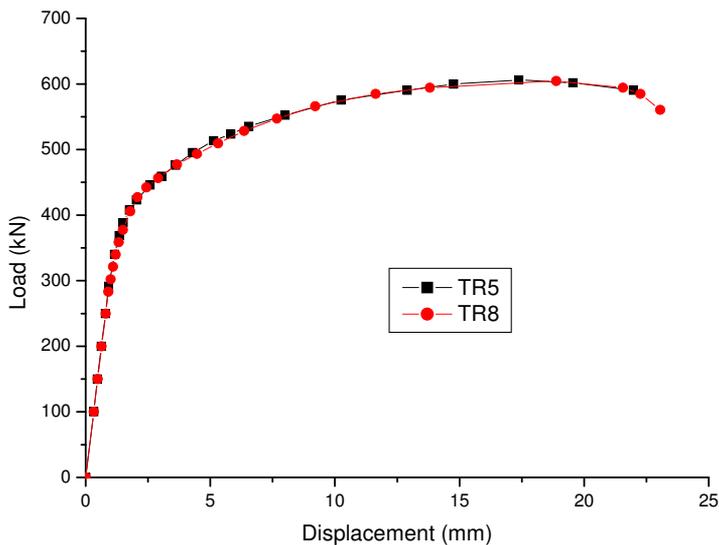
Figure 14. Effect of concrete grade.

Specimen	Yield bearing capacity			Ultimate bearing capacity		
	P_y^e (kN)	P_y^d (kN)	P_y^d/P_y^e	P_u^e (kN)	P_u^d (kN)	P_u^d/P_u^e
TR1	361.9	582.6	1.61	505.8	810.8	1.60
TR2	350.7	466.1	1.33	500.9	648.6	1.29
TR3	337.5	278.8	0.83	462.8	388.0	0.84
TR4	396.4	335.3	0.85	538.9	472.2	0.88
TR5	407.8	335.3	0.82	606.1	472.2	0.78
TR6	361.9	466.1	1.29	504.4	648.6	1.29
TR7	416.7	554.3	1.33	610.0	780.6	1.28
TR8	405.7	335.3	0.83	604.7	472.2	0.78

Table 6. Bearing capacity comparison.

(5) *Cantilever length of diaphragm.* In the case of specimens TR5, and TR7, dimensions and material properties are the same except for the cantilever length h_d of diaphragm, which is 25 mm for TR5 and 45 mm for TR7. Figure 13 shows the load-displacement comparison among specimens TR5 and TR7. It can be seen that the change of cantilever length of diaphragm from 25 mm to 45 mm does not have any obvious influence in failure load and ductility of specimens TR5 and TR7.

(6) *Concrete.* In the case of specimens TR5 and TR8, dimensions and material properties are the same except for the grade of concrete, which is C40 for TR5 and C20 for TR8. Figure 14 shows the load-displacement comparison between specimens TR5 and TR8. It can be seen that the change of grade of concrete from C40 to C20 does not have a noticeable influence on the failure load and ductility of specimens TR5 and TR8.

Bearing capacity comparison. Table 6 presents the experimentally obtained yield tensile capacity P_y^e and ultimate tensile capacity P_u^e of the specimens together with the corresponding computed values P_y^d and P_u^d using (4). For the yield tensile capacity, the difference between experimental results and calculated values ranges from 15% to 61%. For the ultimate tensile capacity, the difference ranges from 12% to 60%. These differences between experimental and calculated values are big. For specimens TR4 and TR5, experiments indicate that an increase of thickness of steel tube increases the bearing capacity. However, the calculated values of TR4 and TR5 are the same because the contribution of the steel tube to the bearing capacity is not reflected in (4). The computed bearing capacity of specimen TR5 is smaller than that of TR7 because specimen TR7 has a larger diaphragm but the experimental bearing capacity of these two specimens is almost the same.

These tests show that the correlation between the predictions of (4) and the experimentally obtained values is rather poor. Therefore there is a need for a better understanding of the yield mechanism of the diaphragm-through joint and an improved method to estimate the yield and ultimate capacity of the joint.

3. Finite element analysis

A three-dimensional finite element model is developed to predict the failure mode, bearing capacity and load-deformation behavior of diaphragm-through joints and compare these predictions with test results.
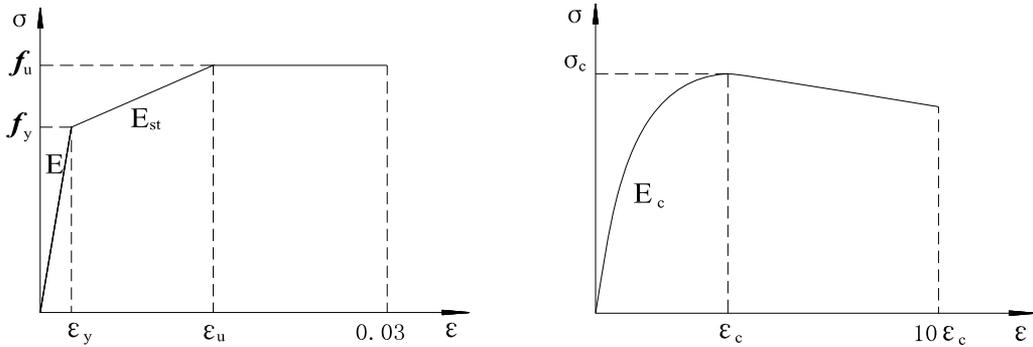
Figure 15. Constitutive law of steel (left) and concrete (right).

Finite element model. The three-dimensional finite element models of diaphragm-through joint specimens were created using the finite element package ANSYS 11.0. The finite element models have the same size and the material properties with the specimens of the static tensile loading experiments as described before.

The main components that need to be modeled in order to simulate the behavior of the diaphragm-through joint are the steel tube, the diaphragm, the beam flange, the infilled concrete and the interface between the concrete and the steel tube. In addition, the choice of the element type, the initial geometric configuration, the boundary conditions and the load application are also important in simulating the diaphragm-through joint and they are also discussed in the following.

(1) *Modeling of the steel tube, diaphragm and beam flange.* The element Solid 95 is used to model steel tube, the diaphragm and the beam flange. The constitutive law is assumed elasto-plastic with Poisson's ratio equal to 0.3. The idealized stress-strain curve [Nie et al. 2008] used in the numerical analysis is shown in Figure 15, left, where $\epsilon_y = f_y/E$, $\epsilon_u = 10(f_u - f_y)/E$.

(2) *Modeling of concrete.* The three-dimensional 8-node element Solid 65 is adopted to model the infilled concrete. The uniaxial stress-strain curve [Chen et al. 2009] shown in Figure 15, right, is adopted with Poisson's ratio equal to 0.2. The constitutive law has two branches. The ascending branch is assumed parabolic up to a strain ϵ_c equal to 0.003 and the descending branch is linear.

(3) *Modeling of the concrete-steel tube interface.* The contact action between the steel and the concrete is modeled by the contact elements Targe 170 and Conta 173. These surface-to-surface contact elements consist of two matching contact faces of steel and concrete elements. The friction between the two faces is maintained as long as the surfaces remain in contact. The coefficient of friction is taken as 0.25. These contact elements allows the surfaces to separate under the influence of tensile force. However, the contact elements are not allowed to penetrate each other.

(4) *Initial geometric configuration.* Since initial geometrical deformations are generally present in practice in diaphragm-through joint specimens, the effect of such deformations is considered in this simulation. For this purpose, a 1% initial deformation resembling the first-order buckling mode has been introduced to the finite element modeling.
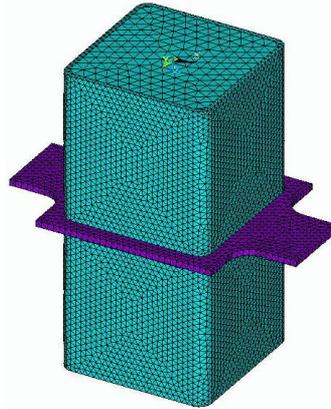
Figure 16. Finite element model.

(5) *Boundary conditions and load application.* The tensile load is transferred through the flange of the steel beam acting on both sides of the diaphragm. To simulate this action one side of the diaphragm was fixed and the tensile load was applied on the other end.

   The load was applied as static uniform load using displacement control at each node of the loaded surface, and the displacement increments were identical to the increments of the experimental investigation. The finite element models are shown in Figure 16.

Numerical results. The failure modes of the diaphragm-through joints, the load-displacement curves and the bearing capacity obtained by the numerical simulation are presented and discussed below.

(1) *Failure modes.* The finite element analysis shows that the failure modes of specimens are similar. The failure modes of specimens TR3 are shown in Figure 17. It can be seen that local buckling appears at the steel tube in agreement with the experimental results.

(2) *Load-displacement curves.* Figure 18 shows the static tensile load-displacement curves compared
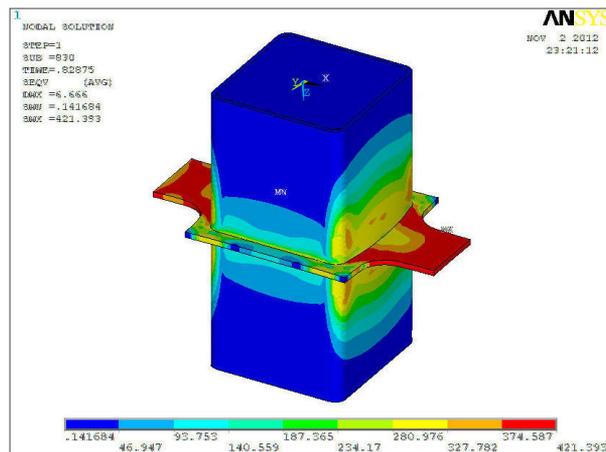
Figure 17. Failure mode of TR3.
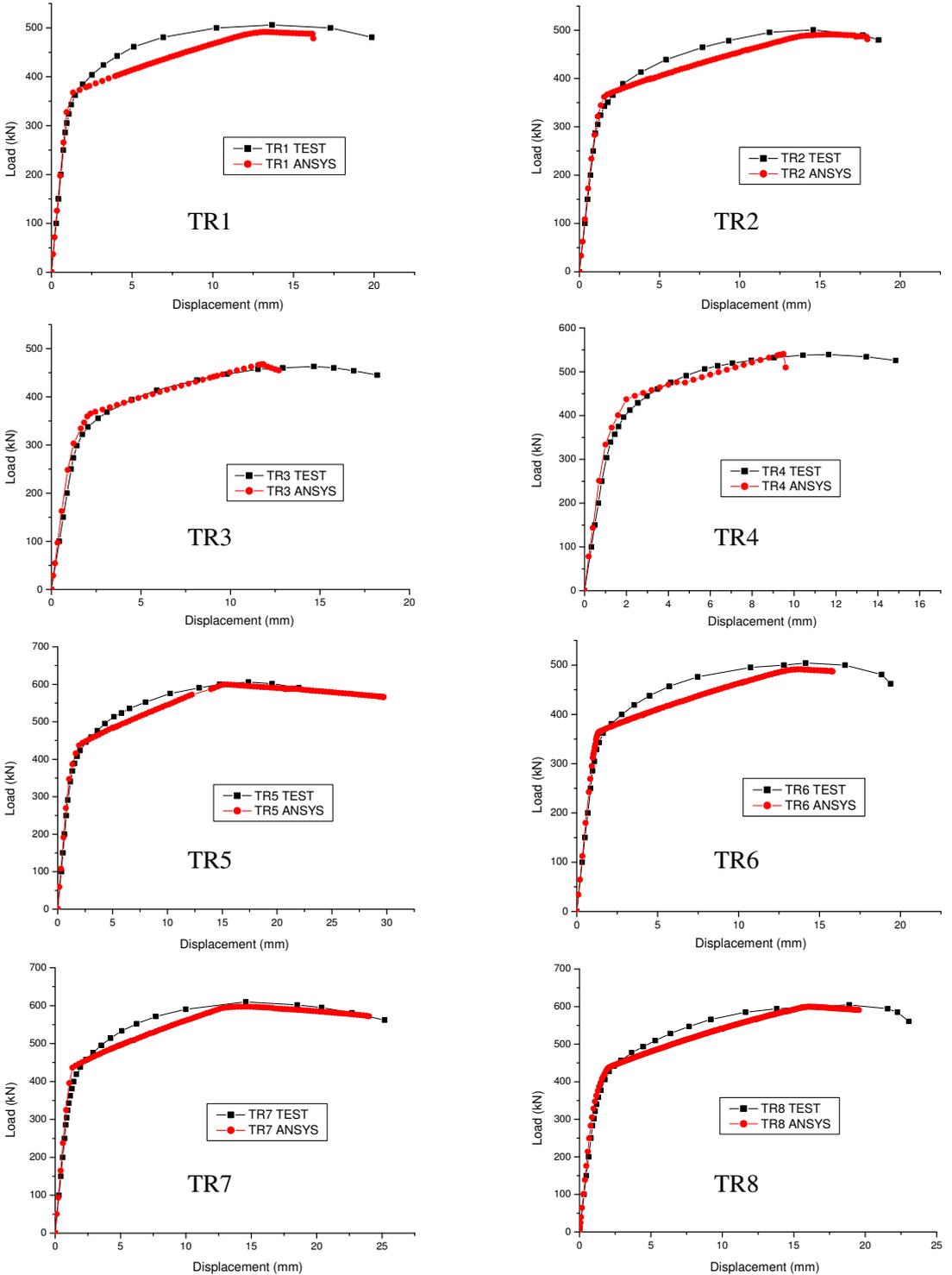
Figure 18. Comparison of load-displacement curves for TR1–TR8.

Specimen	Yield bearing capacity			Ultimate bearing capacity		
	P_y^e (kN)	P_y^f (kN)	P_y^f/P_y^e	P_u^e (kN)	P_u^f (kN)	P_u^f/P_u^e
TR1	361.9	367.4	1.02	505.8	514.6	1.02
TR2	350.7	362.2	1.03	500.9	512.3	1.02
TR3	337.5	347.7	1.03	462.8	474.4	1.03
TR4	396.4	413.5	1.04	538.9	557.4	1.03
TR5	407.8	421.5	1.03	606.1	596.3	0.98
TR6	361.9	367.5	1.02	504.4	517.5	1.02
TR7	416.7	436.3	1.05	610.0	597.2	0.98
TR8	405.7	419.2	1.03	604.7	595.4	0.98

Table 7. Comparison of load-displacement curves.

with the experimental results of specimens. The load-displacement curves obtained by numerical simulation for all the diaphragm-through joints exhibited linear elastic behavior at the initial stage followed by inelastic behavior when the load was further increased. All load-displacement curves are in good agreement with the experimental ones.

(3) *Bearing capacity.* The yield load P_y^f and the ultimate load P_u^f obtained by the above curves are shown in Table 7, and compared with experimental results. For the yield tensile capacity, the difference between experimental and FE results ranges from 2% to 5%. For the ultimate tensile capacity, it ranges from 2% to 3%. It can be concluded that the finite element analysis results and experimental results are in good agreement and thus finite element analysis will give reliable predictions.

4. Yield mechanism

The load transfer mechanism. The finite element analysis and the static tensile loading experiment show that, as the load increases, the load is transferred to the tube and the concrete core. The stress contour of specimen TR3 at failure is shown in Figure 19. It can be seen that there is a large stress distribution
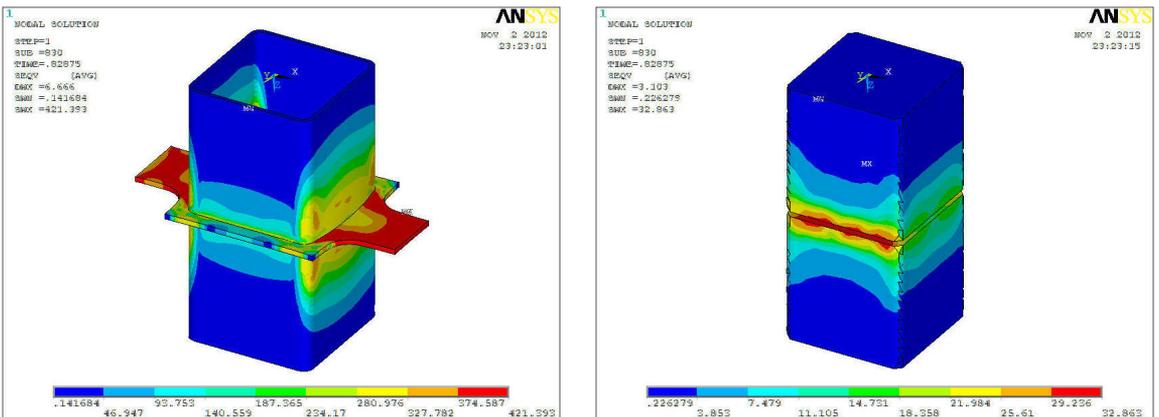
Figure 19. Stress contour of TR3: steel tube and diaphragm (left); concrete (right).
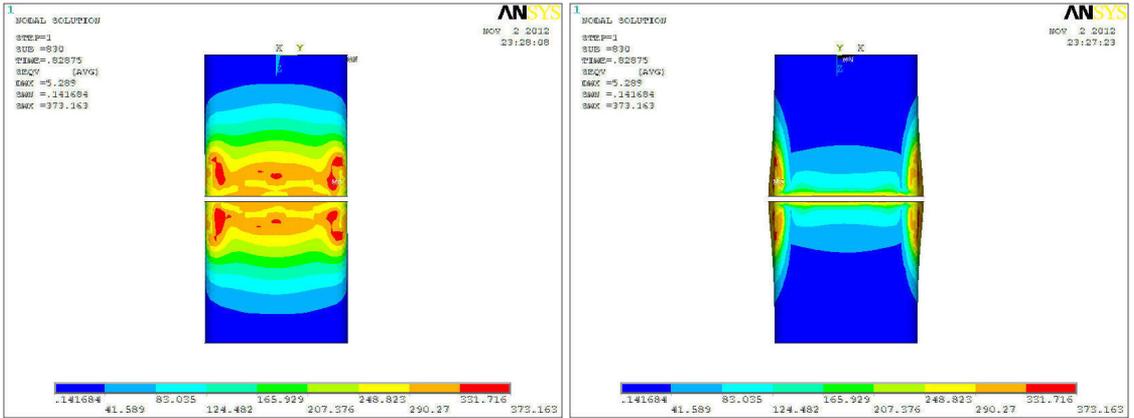
Figure 20. Stress contour in steel tube of TR3: façade (left) and side (right).

zone in the diaphragm and the nearby steel tube while the stress level of the concrete core is lower with a smaller distribution zone. It seems that the tensile load from the steel beam flange is transferred mainly to the square steel tube and the diaphragm.

The yield mechanism of the steel tube. The distribution of the plastic zone in the steel tube of specimen TR3, as obtained by the finite element analysis, is shown in Figure 20. The stress level of the steel tube is higher along the loading direction with a larger distribution area, while in the perpendicular direction the stress level is lower with a smaller distribution area. Plastic zone appears mainly in the intersection of steel tube and diaphragm. Similar results were obtained for the other specimens.

Based on these results a rational procedure for the calculation of the tensile load carried by the steel tube is the yield line model shown in Figure 21.

Let M_{yw} and M_{yc} be the yield moment per unit length of the butt weld and the steel tube respectively and $M_{ya} = \min\{M_{yw}, M_{yc}\}$. By the principle of virtual work $(\partial P_y^c / \partial X = 0)$, the distance X is

$$X = \sqrt{(D + Y - t_c)Y/2}. \tag{5}$$
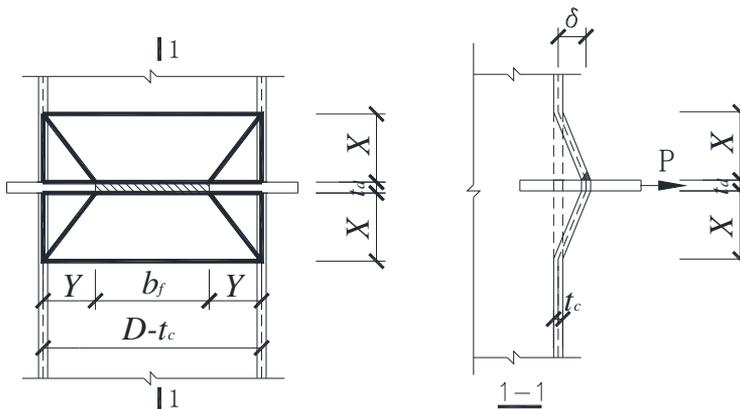
Figure 21. Calculation model of yield lines for steel tube.
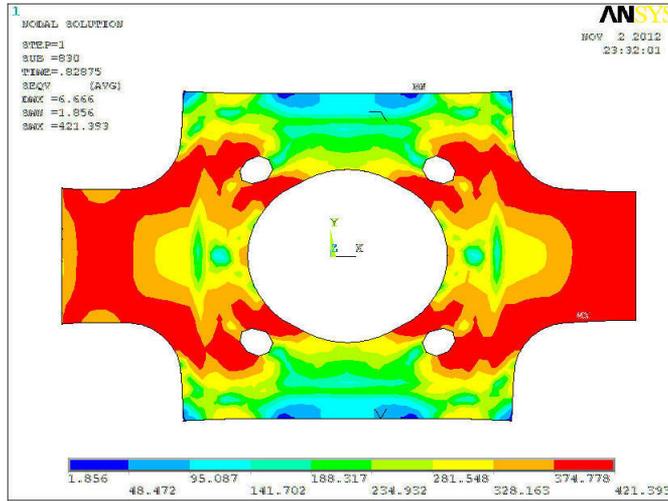
Figure 22. Stress contour in diaphragm of TR3.

And then

$$P_c^y = \frac{4(M_{ya} + M_{yc})X}{Y} + \frac{4M_{yc}(D + Y - t_c)}{X} \tag{6}$$

where D is the width of the tube and t_c is the thickness of the walls of the tube.

The yield mechanism of the diaphragm. The stress distribution of the plastic zone in the diaphragm is shown in Figure 22. The stress level of the diaphragm is higher along the loading direction. In the perpendicular direction the stress level is lower, especially in the cantilevered section. From the stress contour of the specimen of Figure 22 as well as the other analyzed specimens, it seems that the tensile load from the flange is mainly transferred to the section of the diaphragm enclosed by the steel tube and a plastic zone appears along the diagonals of the cross-section lines enclosed by the tube.

Based on these observations a computation model of the yielding mechanism of the diaphragm is shown in Figure 23 where it is assumed that yielding will take place along the diagonals of the diaphragm [Lu 1997].

The yield tensile strength P_d^y can be calculated from Figure 23 using

$$P_d^y = \sqrt{2}t_d f_{yd}(l_2 + l_1/2) \tag{7}$$

where t_d is the thickness of the diaphragm and f_{yd} is the yield stress of the diaphragm.

Verification of the analytical method. The total ultimate bearing capacity of diaphragm-through joint under static tensile load is given by (6) and (7) if the yield strength is substituted by the ultimate

$$P_u = \frac{4(M_{ua} + M_{uc})X}{Y} + \frac{4M_{uc}(D + Y - t_c)}{X} + \sqrt{2}t_d f_{ud}(l_2 + l_1/2). \tag{8}$$

In order to verify the proposed analytical method, a comparison, as exhibited in Table 8, is made between the static tensile experimental results of diaphragm-through joints and the calculated ultimate tensile capacity P_u. For specimens TR3, TR4, T5, TR7 and TR8 with failure of joint, P_u is calculated using (8).
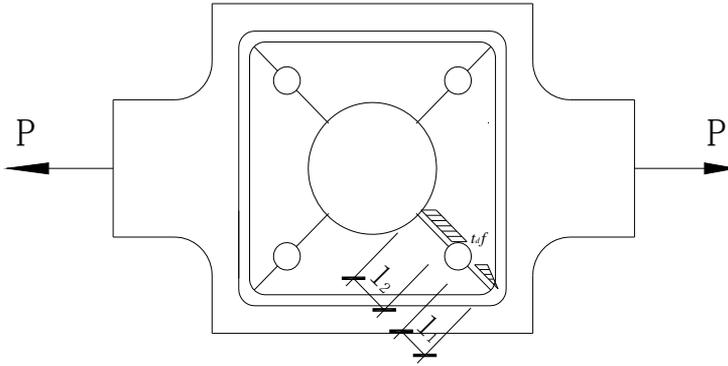
Figure 23. Calculation model of yield lines for diaphragm.

Specimen		Ultimate bearing capacity		
		P_u^e (kN)	P_u (kN)	P_u/P_u^e
Failure of flange	TR1	505.8	526.8	1.04
	TR2	500.9	526.8	1.05
	TR6	504.4	526.8	1.04
Failure of joint	TR3	462.8	425.5	0.92
	TR4	538.9	482.8	0.90
	TR5	606.1	580.4	0.96
	TR7	610.0	580.4	0.95
	TR8	604.7	580.4	0.96

Table 8. Comparison of test and computed bearing capacities.

For specimens TR1, TR2 and TR6 with failure of flange, $P_u = f_u \cdot t \cdot b_f$, where, f_u is the ultimate strength of the flange, t is the thickness of the flange and b_f is the width of the flange. According to (8), the calculated ultimate tensile capacity P_u of specimens TR1, TR2 and TR6 is 559.3 kN, 529.6 kN and 529.6 kN respectively, which is larger than $P_u = f_u \cdot t \cdot b_f$. As shown in Table 8, the computed capacities are in good agreement with the experimental.

5. Conclusions

Through static tensile loading experiments and finite element simulations, the mechanical properties and the bearing capacity of diaphragm-through joint of concrete-filled square steel tubular column under static tensile load are investigated in this paper.

The static tensile loading experiments show that there are two types of failure modes: the failure of the flange and the failure of the joint. The contribution of the infilled concrete is small and can be neglected.

Comprehensive comparison of finite element analysis and experimental results are in good agreement. Based on the findings of this analytical and experimental investigation, a rational computational procedure for the evaluation of the ultimate capacity is proposed. This procedure takes into account the

contribution of the diaphragm-through as well as the steel tube which, unlike the contribution of the infilled concrete, was found to be considerable.

The predictions of the proposed procedure are in good agreement with the experimental data of this investigation.

Acknowledgments

References

[Chen et al. 2006] Y.-Y. Chen, G. Li, L. Zhuang, M.-X. Huang, and J. Li, "Experimental study on the seismic performance of diaphragm through type joint connecting H beam and tube column in steel frame", *Prog. Steel Build. Struct.* **8**:1 (2006), 23–30. In Chinese.

[Chen et al. 2009] Z.-H. Chen, B. Rong, and A. Fafitis, "Axial compression stability of a crisscross section column composed of concrete-filled square steel tubes", *J. Mech. Mater. Struct.* **4**:10 (2009), 1787–1799.

[Fukumoto and Morita 2005] T. Fukumoto and K. Morita, "Elasto-plastic behavior of panel zone in steel beam-to-concrete filled steel tube column moment connections", *J. Struct. Eng.* (*ASCE*) **131**:7 (2005), 1841–1853.

[Han et al. 2003] L. H. Han, Y. F. Yang, and Z. Tao, "Concrete-filled thin-walled steel SHS and RHS beam-columns subjected to cyclic loading", *Thin-Walled Struct.* **41**:9 (2003), 801–833.

[Han et al. 2008] L. H. Han, W. D. Wang, and X. L. Zhao, "Behaviour of steel beam to concrete-filled SHS column frames: finite element model and verifications", *Eng. Struct.* **30**:6 (2008), 1647–1658.

[Jiang et al. 2009] X.-L. Jiang, J.-K. Miao, and Z.-H. Chen, "Experiment on seismic performance of diaphragm-through joint between concrete-filled square steel tubular column and steel beam", *J. Tianjin Univ.* **42**:3 (2009), 194–200. In Chinese.

[Lu 1997] L. H. Lu, *The static strength of I-beam to rectangular hollow section column connections*, Ph.D. thesis, Delft University, Delft, 1997, http://repository.tudelft.nl/view/ir/uuid:80f96639-3f74-4231-8dab-af93cdb97a5f.

[Matsui 1985] C. Matsui, "Strength and behavior of frames with concrete filled square steel tubular columns under earthquake loading", pp. 143–146 in *Proceedings of the International Specialty Conference on Concrete Filled Steel Tubular Structures* (Harbin, 1985), 1985.

[Morino and Tsuda 2002] S. Morino and K. Tsuda, "Design and construction of concrete-filled steel tube column system in Japan", *Earthq. Eng. Eng. Seismol.* **4**:1 (2002), 51–73.

[Nie et al. 2005] J.-G. Nie, K. Qin, and G.-B. Zhang, "Experimental research and theoretical analysis on flexural capacity of connections for concrete-filled steel square tubular columns with inner diaphragms", *J. Archit. Civ. Eng.* **22**:1 (2005), 42–49. In Chinese.

[Nie et al. 2008] J.-G. Nie, K. Qin, and C. S. Cai, "Seismic behavior of connections composed of CFSSTCs and steel-concrete composite beams — finite element analysis", *J. Constr. Steel Res.* **64**:6 (2008), 680–688.

[Nishiyama et al. 2004] I. Nishiyama, T. Fujimoto, and T. Fukumoto, "Inelastic force-deformation response of joint shear panels in beam-column moment connections to concrete-filled tubes", *J. Struct. Eng.* (*ASCE*) **130**:2 (2004), 244–252.

[Park et al. 2010] S. H. Park, S. M. Choi, Y. S. Kim, Y. Park, and J. H. Kim, "Hysteresis behavior of concrete filled square steel tube column-to-beam partially restrained composite connections", *J. Constr. Steel Res.* **66**:7 (2010), 9433–953.

[Ricles et al. 2004] J. M. Ricles, S. W. Peng, and L. W. Lu, "Seismic behavior of composite concrete filled steel tube column-wide flange beam moment connections", *J. Struct. Eng.* (*ASCE*) **130**:2 (2004), 223–232.

[Sasaki et al. 1995] S. Sasaki, M. Teraoka, K. Morita, and T. Fujiwara, "Structural behavior of concrete-filled square tubular column with partial penetration weld corner seam to steel H-beam connections", pp. 33–40 in *Structural steel: PSSC '95, 4th*

Pacific Structural Steel Conference: 2, Structural connections (Singapore, 1995), edited by N. E. Shanmugam and Y. S. Choo, Pergamon, Oxford, 1995.

[Zhou et al. 2005] T. H. Zhou, S. F. Nie, L. F. Lu, and B. K. He, "Design of concrete-filled square tube column and steel beam joint with internal diaphragms", *J. Build. Struct.* **26**:5 (2005), 23–29. In Chinese.

RONG BIN: rongbin2010@hotmail.com
School of Civil Engineering and Key Laboratory of Coast Civil Structure Safety, Tianjin University, Tianjin, 300072, China

CHEN ZHIHUA: zhchen@tju.edu.cn
School of Civil Engineering and Key Laboratory of Coast Civil Structure Safety, Tianjin University, Tianjin 300072, China

ZHANG RUOYU: zryu@tju.edu.cn
School of Naval and Ocean Engineering, Tianjin University, Tianjin 300072, China

APOSTOLOS FAFITIS: fafitis@asu.edu
Department of Civil and Environmental Engineering, Arizona State University, Tempe, AZ 85287, United States

YANG NAN: yangnangre@gmail.com
School of Civil Engineering, Tianjin University, Tianjin 300072, China

JOURNAL OF MECHANICS OF MATERIALS AND STRUCTURES

Journal of Mechanics of Materials and Structures